

# Polarization-dependent effects in point-by-point fiber Bragg gratings enable simple, linearly polarized fiber lasers

Nemanja Jovanovic,<sup>1\*</sup> Jens Thomas,<sup>2</sup> Robert J. Williams,<sup>1</sup> M. J. Steel,<sup>1</sup> Graham D. Marshall,<sup>1</sup> Alexander Fuerbach,<sup>1</sup> Stefan Nolte,<sup>2</sup> Andreas Tünnermann,<sup>2</sup> and Michael J. Withford<sup>1</sup>

<sup>1</sup>*MQ Photonics Research Centre, Centre for Ultrahigh bandwidth Devices for Optical Systems (CUDOS), Department of Physics and Engineering, MQ Photonics Research Centre, Macquarie University, North Ryde, New South Wales 2109, Australia*

<sup>2</sup>*Institute of Applied Physics, Friedrich-Schiller-University, Max-Wien-Platz 1, D-07743 Jena, Germany*

\*Corresponding author: [njovanov@ics.mq.edu.au](mailto:njovanov@ics.mq.edu.au)

**Abstract:** Fiber Bragg gratings inscribed with a femtosecond laser using the point-by-point (PbP) technique have polarization dependent grating strength (PDGS) and exhibit birefringence. In this paper we quantify the dependence of these two properties on the ellipticity, position in the core and size of the micro-voids at the center of each refractive index modulation. We demonstrate that the effective modal index for type II gratings written with a femtosecond laser using the PbP method must be lower than that of the pristine fiber, and for the first time associate an axis with a polarization such that the long axis of the elliptically-shaped index modulations corresponds to the slow axis of the gratings. We exploit the PDGS of two gratings used as frequency-selective feedback elements as well as appropriate coiling, to realize a linearly-polarized fiber laser with a low birefringence fiber cavity. We show that the polarization-dependent grating strength is a function of the writing pulse energy and that only gratings optimized for this property will linearly polarize the fiber laser. The fiber lasers have high extinction ratios (>30 dB) for fiber lengths of up to 10 m and very stable polarized output powers (<0.5% amplitude fluctuations) in the range of 20-65 mW at 1540 nm. This method of polarization discrimination allows the realization of highly robust and simplified linearly polarized fiber lasers.

©2009 Optical Society of America

**OCIS codes:** (060.3735) Fiber Bragg gratings; (230.5440) Polarization selective devices; (320.2250) Femtosecond phenomena; (060.3510) Fiber lasers.

---

## References and links

1. Y. Lai, A. Martinez, I. Khrushchev and I. Bennion, "Distributed Bragg reflector fiber laser fabricated by femtosecond laser inscription," *Opt. Lett.* **31**, 1672-1674 (2006).
2. E. Wikszak, J. Thomas, J. Burghoff, B. Ortaç, J. Limpert, S. Nolte, U. Fuchs, and A. Tünnermann, "Erbium fiber laser based on intracore femtosecond-written fiber Bragg grating," *Opt. Lett.* **31**, 2390-2392 (2006).
3. N. Jovanovic, A. Fuerbach, G. D. Marshall, M. J. Withford, and S. D. Jackson, "Stable high-power continuous-wave Yb<sup>3+</sup>-doped silica fiber laser utilizing a point-by-point inscribed fiber Bragg grating," *Opt. Lett.* **32**, 1486-1488 (2007).
4. C. W. Smelser, S. J. Mihailov and D. Grobnc, "Formation of Type I-IR and Type II-IR gratings with an ultrafast IR laser and a phase mask," *Opt. Express* **13**, 5377-5386 (2005).
5. A. Martinez, I. Y. Khrushchev, and I. Bennion, "Thermal properties of fiber Bragg gratings inscribed point-by-point by infrared femtosecond laser," *Electron. Lett.* **41**, 176-177 (2005).
6. N. Jovanovic, M. Åslund, A. Fuerbach, S. D. Jackson, G. D. Marshall, and M. J. Withford, "Narrow linewidth, 100W cw Yb<sup>3+</sup>-doped silica fiber laser with a point-by-point Bragg grating inscribed directly into the active core," *Opt. Lett.* **32**, 2804-2806 (2007).
7. N. Jovanovic, G. D. Marshall, A. Fuerbach, G. E. Town, S. Bennetts, D. G. Lancaster and M. J. Withford, "Highly-narrow linewidth, CW, all-fiber oscillator with a switchable linear polarization," *Photon. Technol. Lett.* **20**, 809-901 (2008).

8. P. Lu, D. Grobnc and S. J. Mihailov, "Characterization of the birefringence in fiber Bragg gratings fabricated with an ultrafast-infrared laser," *IEEE J. Lightwave Technology* **25**, 779-786 (2007).
9. Y. Lai, K. Zhou, K Sugden, and I. Bennion, "Point-by-point inscription of first order fiber Bragg grating for C band applications," *Opt. Express* **15**, 18318-18325 (2007).
10. E. Wikszak, J. Thomas, S. Klingebiel, B. Ortaç, J. Limpert, S. Nolte, and A. Tünnermann, "Linearly polarized ytterbium fiber laser based on intracore femtosecond-written fiber Bragg gratings," *Opt. Lett.* **32**, 2756-2758 (2007).
11. A. Martinez, M. Dubov, I.Y. Khrushchev, and I. Bennion, "Photoinduced modifications in fiber gratings inscribed directly by infrared femtosecond irradiation," *Photon. Technol. Lett.* **18**, 2266-2268 (2006).
12. C. B. Schaffer, A.O. Jamison and E. Mazur, "Morphology of femtosecond laser-induced structural changes in bulk transparent materials," *Appl. Phys. Lett.* **84**, 1441-1443 (2004).
13. Comsol, Perpendicular Hybrid Mode Waves Package, [www.comsol.com](http://www.comsol.com)
14. RSoft, BandSOLVE, [www.rsoftdesign.com](http://www.rsoftdesign.com)
15. I. H. Malitson, "Interspecimen comparison of the refractive index of fused silica," *J. Opt. Soc. Am.* **55**, 1205-1209 (1965).
16. SMF 28e specification sheet, <http://www.corning.com/WorkArea/showcontent.aspx?id=15535>
17. I. K. Hwang, Y. H. Lee, K. Oh and D.N. Payne, "High birefringence in elliptical hollow optical fiber," *Opt. Express* **20**, 1916 (2004).
18. R. B. Dyott, *Elliptical fiber waveguides*, (Artech House, London, 1995).
19. M. J. Steel and R. M. Osgood, Jr, "Elliptical hole photonic crystal fibers," *Opt. Lett.* **26**, 229-231 (2001).
20. T. Erdogan, "Fiber grating spectra," *IEEE J. Lightwave Technol.* **15**, 1277-1294 (1997).
21. S. Juodkazis, H. Misawa, T. Hashimoto, E. Gamaly, B. Luther-Davies, "Laser-induced microexplosion confined in a bulk of silica: Formation of nanovoids," *Appl. Phys. Lett.* **88**, 201909 (2006)
22. D. Homoele, S. Wielandy, A. L. Gaeta, N. F. Borrelli and C. Smith, "Infrared photosensitivity in silica glasses exposed to femtosecond laser pulses," *Opt. Lett.* **24**, 1311-1313 (1999).
23. F. Dürr, H. G. Limberger, R. P. Salathe, F. Hindle, M. Douay, E. Fertein, and C. Przygodski, "Tomographic measurement of femtosecond-laser induced stress changes in optical fibers," *Appl. Phys. Lett.* **84**, 4983-4985 (2004).

---

## 1. Introduction

In recent times, fiber Bragg gratings (FBGs) inscribed by either the point-by-point (PbP) or phase mask (PM) technique using a femtosecond laser have received much attention in their applications as frequency-selective feedback elements in fiber lasers. This is because they offer many advantages over FBGs written with UV lasers. For example, they offer direct inscription into non-photosensitive rare-earth doped fibers [1-3] which increases fiber laser robustness because it minimizes the requirement for splices and reduces losses due to mode mismatch. Other advantages include thermal stability at temperatures of up to 800°C [4, 5] which allows for high power scaling of fiber lasers [6] and reasonable wavelength tunability with temperature [1, 3], and narrow laser linewidths [1, 7]. Finally, they exhibit significant polarisation dependent grating strength (PDGS) as compared to gratings written with nanosecond lasers and UV wavelengths [8, 9]. This last property has been exploited in a PbP FBG to create a linearly-polarized, low birefringence fiber laser (extinction ratio >40 dB), albeit 31 mm in length with a very low output power of 45  $\mu$ W [1]. The mechanism for polarization discrimination in this case is the difference in cavity losses for the two orthogonal states of linear polarization as defined by the grating. Over these short fiber lengths, it is possible to keep the fiber straight and therefore maintain the laser's state of polarization. Longer fiber lasers with output powers of several hundred milliWatts have been demonstrated with femtosecond inscribed gratings but they incorporated polarization-maintaining (PM) fiber in their cavities [7, 10]. It is often desirable to use low birefringence fibers instead of PM fibers to create polarized fiber lasers because they are cheaper, more readily available and reduce any unnecessary complication to the laser systems in terms of fiber mismatches and splicing difficulties. Therefore, in order to increase the output power of fiber lasers utilizing low birefringence fibers and exploiting this type of polarization discrimination, it is necessary to significantly increase the cavity length from the 31 mm already demonstrated. Typically this will come at the expense of a reduced extinction ratio as the low birefringence cavity will invariably act to depolarize the fiber laser and hence it is not intuitive that scaling to high powers with high polarization extinction ratios is possible.

In this body of work, we demonstrate that the polarization-dependent effects associated with PbP FBGs are a result of the elliptical shape of the refractive index modulations (RIMs)

that constitute the FBG. We show that the ellipticity, size and vertical offset of the RIMs from the centre of the core are the key parameters that determine the grating's overall birefringence and the difference in grating reflectivity for two orthogonally polarized modes. For the first time, the spatial axes of the grating are assigned to a polarization-dependent transmission spectrum. We further show that the effective indices of a mode with a PbP FBG inscribed in the fiber are lower than that of the pristine fiber, which is consistent with a reduction in the average core index due to the formation of a micro-void at the centre of the RIMs [11, 12]. Finally, we use two PbP FBGs optimized by varying the writing pulse energy for maximum PDGS, as the high reflector (HR) and output coupler (OC) for a low birefringence fiber laser cavity, and elucidate the linearly-polarized nature of the laser. Extinction ratios of the order of 30 dB were observed for cavity lengths up to 10 m when coiling of the cavity was employed. This technique for polarization discrimination opens the way for creating highly simplified and robust linearly-polarized fiber lasers.

## 2. Experiment

### 2.1 Polarization-dependent grating strength in PbP FBGs

In order to fabricate the FBGs, the polymer coating was stripped off SMF-28e fiber, and the fiber was threaded through a glass ferrule positioned such that the core of the fiber was at the focus of a 0.8 N.A., 20 $\times$  oil-immersion objective lens used for grating writing. The output face of the objective lens, the fiber and the ferrule were all immersed in index matching oil. A high-precision air-bearing translation stage was used to pull the fiber through the ferrule at a constant velocity as femtosecond laser pulses inscribed the refractive index modulations, which make up the grating. Uniform Bragg gratings were written with pulse energies between 120 and 250 nJ, for a pulse duration of <110 fs, generated by a regeneratively-amplified Ti:Sapphire femtosecond laser operating at 800 nm with a 1 kHz repetition rate. Second-order gratings with target Bragg wavelengths,  $\lambda_B$ , in the range of 1520-1570 nm, were inscribed, with the period,  $\Lambda_p$ , given by  $\Lambda_p = \lambda_B / \bar{n} = 1.050$ - $1.085$   $\mu\text{m}$  respectively, where  $\bar{n}$  is the effective index of propagation for the fundamental mode of the fiber. Second order gratings were used in order to minimize the overlap between neighboring RIMs since the diameter of the focal spot in the core of the fiber was of the order of 1  $\mu\text{m}$ . All FBGs were 5 mm long.

A swept wavelength system (SWS) from JDS Uniphase, was used to probe the gratings. The system consists of a narrow linewidth (100 kHz), external cavity laser diode that is continuously swept from 1520-1570-nm, while the detection is carried out by a photodiode which acquires data every  $\sim 3\text{pm}$ . An external polarizing module was used to generate the required states of polarization. The system measured the insertion loss across four states of polarization (3 linear and 1 circular) and from that calculated the maximum and minimum insertion losses across all possible states of polarization. For several gratings we also measured the transmission spectra by using a white light source, a U-bench with a linear polarizer and an optical spectrum analyzer. By keeping the fiber pigtail between the U-bench and the grating short ( $\sim 15$  cm) and straight, the state of polarisation launched was maintained up to the grating. In order to determine the orientation of the polarizer with respect to the grating axes, the gratings were imaged with an optical microscope before hand, and the long axis of the gratings was marked. It was determined that when the polarizer was oriented parallel to the markers (long axis of the grating) there was a minimum grating reflectivity and when it was orthogonal to the markers there was a maximum in grating reflectivity (similar to those in Fig. 1(a)). It was determined that the SWS's spectra for polarization states with extremal loss were consistent with the transmission properties for two orthogonal states of linear polarization. Thus, for simplicity, all further measurements were made with the SWS.

Typical transmission spectra of a PbP FBG with PDGS are shown in Fig. 1(a).

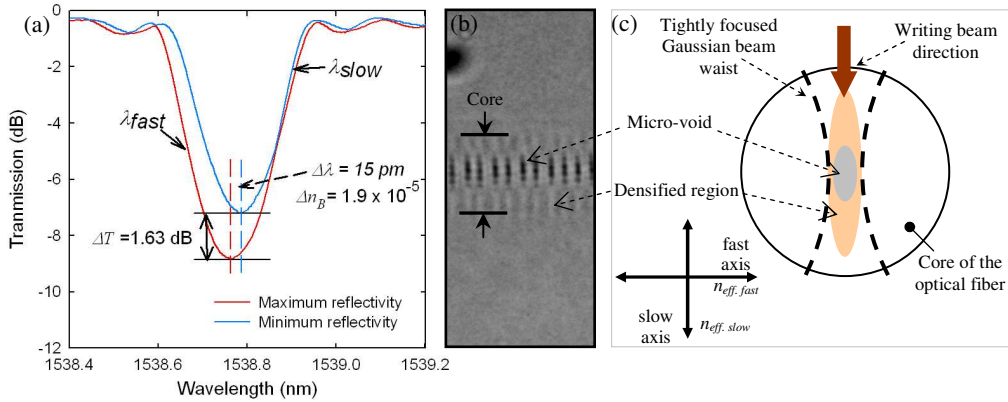


Fig. 1. (a). Transmission spectra for two orthogonal states of linear polarization for a PbP FBG written with 160 nJ. (b). Transmission image of a typical PbP FBG taken orthogonal to the writing direction. (c). Schematic diagram of the cross section of a single RIM in the PbP FBG.

Even though the wavelength splitting was much smaller than the bandwidth of the grating it was 4 times greater than the resolution of the system ( $\sim 12$  pm) and was very reproducible over several scans. From the wavelength separation between the two grating peaks, we infer birefringence  $\Delta n_B = \Delta \lambda_S / \lambda_p$ , where  $\Delta \lambda_S$  is the difference between the two Bragg wavelengths. It was determined that the shorter wavelength peak, denoted as  $\lambda_{fast}$  in Fig. 1(a), is associated with the polarization state perpendicular to the writing direction while the  $\lambda_{slow}$  peak, which has a higher effective refractive index, is associated with the polarization parallel to the writing direction (see Fig. 1(c)). The schematic of the refractive index profile of a single modulation is based on micrographs of the gratings as shown in Fig. 1(b). Since the grating strength for  $\lambda_{fast}$  is greater than that for  $\lambda_{slow}$ , then  $|\Delta n_{fast}| > |\Delta n_{slow}|$ , where  $\Delta n$  is the effective refractive index contrast of the grating or the “AC” component of the refractive index profile. (It is important to note that the RIMs are not uniform across the entire core and therefore the index contrast is a spatially varying function. However, the fiber mode samples this function and the averaged or effective grating index contrast results in the observed Bragg dips in transmission.) On the other hand, from the Bragg condition, we must have  $n_{eff. fast} < n_{eff. slow}$ , where  $n_{eff.}$  is the effective index for the mode propagating in the grating. The difference of these quantities from the effective index of the pristine fiber is associated with the “DC” component of the index profiles. However, since the “DC” and “AC” terms are induced by the same RIM, they must be proportional. This implies that the two conditions  $|\Delta n_{fast}| > |\Delta n_{slow}|$  and  $n_{eff. fast} < n_{eff. slow}$  can only be satisfied simultaneously if the  $\Delta n$ 's are negative in direction and hence the  $n_{eff.}$ 's are lower than that of the background material. This observation suggests the formation of micro-voids at the core of the refractive index modulations which are either filled with a vacuum or air (index of 1) and for the first time assigns a transmission spectrum with a grating axis [12]. Indeed micro-void formation has been demonstrated in bulk glasses [12] with similar focusing geometries and pulse energies as those used to inscribe these FBGs.

## 2.2 Modeling of polarization-dependent effects from RIMs in PbP FBGs

The goal was to quantitatively determine what parameters of a RIM of a PbP FBG effect the birefringence and difference in reflectivity for two orthogonal states of linear polarization. The mode field profiles and respective effective indices for the two orthogonal states of linear polarization were numerically computed, for SMF-28e fiber with a RIM of a PbP FBG inscribed into the core. From this the birefringence,  $\Delta n_B$ , was determined. The computed mode fields were used in the coupled mode theory for fibers to calculate the coupling coefficients for the two orthogonal states of polarization with the grating and hence calculate the difference in reflectivity between them.

Modeling of the polarization-dependent effects was conducted using a commercial finite element analysis tool (COMSOL) [13]. The results were checked using a plane wave expansion calculation [14]. A CAD idealization of the cross-sectional refractive index profile was constructed as depicted in Fig. 2(a), assuming elliptical regions for the void (with void area,  $A_v = \pi(h_v \times w_v)/4$ , where  $h_v$  and  $w_v$  are the void height and width respectively) and densification ( $h_d$  and  $w_d$  are the height and width of the densification respectively). To estimate a reasonable range of parameter space for the dimensions of the RIMs to be modeled, measurements of the dimensions of the voids and densifications were taken from microscope images of typical PbP FBGs, similar to Fig. 1(b). Since our gratings are typically inscribed into the core of SMF-28e fiber, the parameters for this fiber were used in the model: a core diameter of 8.3  $\mu\text{m}$ , cladding refractive index of 1.44421 at  $\lambda = 1550$  nm (index of pure fused silica) and a 0.36 % index step between the core/clad interface [15, 16].

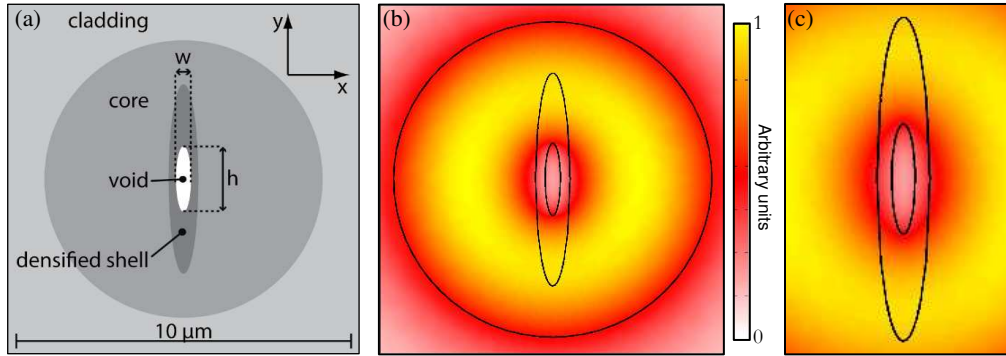


Fig. 2. (a). CAD idealization of the cross-sectional refractive index profile of a RIM in a PbP FBG. (b) Energy flux profile for the  $x$ -polarized mode. (c) Energy flux profile for the  $y$ -polarized mode, magnified around the void region.

To simplify the calculations, the densification is initially neglected and the birefringence and difference in grating strength are evaluated for the void only. This is reasonable since the magnitude of the index change of the void is at least one order of magnitude greater than that of the densification (as elucidated in section 2.3), and the magnitude and distribution of the index profile of the densification are the least well-known parameters. Thus ignoring the densified region should capture most of the physics and should not significantly affect the agreement with experiment. This is confirmed later.

For the mode calculations, we treated the modification as  $z$ -invariant, rather than periodic along the length of the core. This was taken into account by rescaling the index of the void,  $n_v = 1$ , by the RIM duty cycle with the mean index of the void,  $n_{mvi}$ , approximated as:

$$n_{mvi} = \frac{1}{A_p} [(w_v \cdot n_v) + (A_p - w_v) \cdot n_{core}], \quad (1)$$

where  $n_{core} = 1.4494$ , is the refractive index of the core in SMF-28e.

Figure 2(b) shows the energy flux profile, (the  $z$ -component of the Poynting vector) for the  $x$ -polarized mode (parallel to fast axis in Fig. 1(c)). From Fig. 2(b) it can be seen that the fundamental Gaussian-like mode of a SMF-28e fiber has changed to a quasi-annular mode in terms of energy distribution. The void has the effect of redistributing the energy of the mode away from the center of the core, but the remaining field samples a lower refractive index leading to an effective index below that of a pristine piece of SMF-28e which is 1.446468. Simultaneously, the light that is expelled from the center of the core is not guided as tightly as it would be without the modification present and therefore the field extends further into the cladding, which also leads to a lower effective index (as observed in Fig. 2.1). The effective indices calculated for the  $x$  and  $y$ -polarized modes were  $n_{eff. x} = 1.445425$  and  $n_{eff. y} = 1.445489$ , which demonstrates that a birefringence with a magnitude of  $\Delta n_B = n_{eff. y} - n_{eff. x} = 6.4 \times 10^{-5}$  is

predicted, which is the same order of magnitude as observed for the FBG in Fig. 1(a). The origin of this birefringence is the different boundary conditions for Maxwell's equations for the  $x$  and  $y$ -polarized modes at the interface of an abrupt index change. Specifically, the  $x$ -polarized mode is discontinuous along the longer (vertical) boundaries of the void while the  $y$ -polarized mode is discontinuous along the shorter (horizontal) boundaries of the void. Also  $n_{eff. y} > n_{eff. x}$ , which is consistent with the assignment of the fast and slow axes in Fig. 1(c) above, and with the established theory of modes of elliptical-core fibers, for which the mode polarized along the major axis ( $y$ -polarized) tends to be of higher effective index. Loosely speaking, one can think of the ellipse as locally being similar to a slab waveguide and the  $y$ -polarized mode is then more TE-like in character than the orthogonal mode [17-19].

In order to determine the difference in reflectivity for the two orthogonally polarized modes,  $\Delta R$ , we applied the coupled mode theory for fiber gratings as outlined in [20]. However, in order to take into account the strong, non-uniform transverse index modulation,  $\Delta n(x,y)$ , we retained all terms in the index modulation given by  $n_{core}^2 - (n_{core} + \Delta n)^2$ . In weak index-contrast gratings, one commonly drops the term in  $\Delta n^2$ . The coefficient expressing the cross-coupling between different modes takes the form

$$\kappa_m = \frac{\pi}{4} \cdot \frac{\omega \epsilon_0}{8m_{mod}} \iint dx dy [2n_{core} \Delta n(x, y) + \Delta n(x, y)^2] \cdot (\mathbf{E}_t \cdot \mathbf{E}_t^*), \quad (2)$$

where  $\mathbf{E}_t$  is the normalized transverse electric field of the mode,  $m$  denotes the order of the resonance (here  $m = 2$ ) and we integrate only over the modified region. The reflectivity,  $R$ , for a uniform grating of length  $L$ , is then given by

$$R = \tanh^2(\kappa_m L). \quad (3)$$

Since the precise parameters of the fibers under study are unknown, to confirm that the above result holds true throughout the relevant parameter space, a scan was conducted to determine the effect of the size of the void on  $\Delta n_B = n_{eff. y} - n_{eff. x}$  and  $\Delta R$ . Figures 3(a) and 3(b) show  $\Delta n_B$  and the difference in the coupling coefficients,  $\Delta \kappa$ , at  $\lambda = 1540$  nm as a function of the void area  $A_v$ , for a number of different ellipticities, defined as  $\eta = h_v/w_v - 1$ , respectively. Note that by this definition a symmetric (circular) void has  $\eta = 0$ . As expected when a symmetric void is modeled, the predicted  $\Delta n_B$  and  $\Delta \kappa$  vanish, since both polarizations see the same perturbation. Both  $\Delta n_B$  and  $\Delta \kappa$  can be seen to increase monotonically with  $\eta$ , but for a fixed ellipticity, there is an optimum void area,  $A_v$  at which they reach a maximum. It is interesting to note however, that the optimum  $A_v$  for a given  $\eta$  is not the same for both  $\Delta n_B$  and  $\Delta \kappa$  and should be taken into account when optimizing FBGs for either of the two properties.

The ellipticity of a given void is predominantly determined by the N.A. of the focusing objective used, as this determines the Rayleigh range and beam waist. Indeed, these results suggest that PbP FBGs written with a 1.4 N.A. oil immersion objective which have been shown to be circularly symmetric [12], would have no  $\Delta n_B$  and  $\Delta \kappa$  and would therefore not be useful for the type of polarization discrimination outlined in the introduction. However by using a 0.45 N.A. oil immersion objective, which has been shown to produce an elliptical RIM with the greatest degree of ellipticity as it has the lowest N.A. and longest working distance, it should be possible to inscribe FBGs with the greatest amount of  $\Delta \kappa$  [12]. On the other hand the extent of the void can be adjusted by varying the writing pulse energy [21].

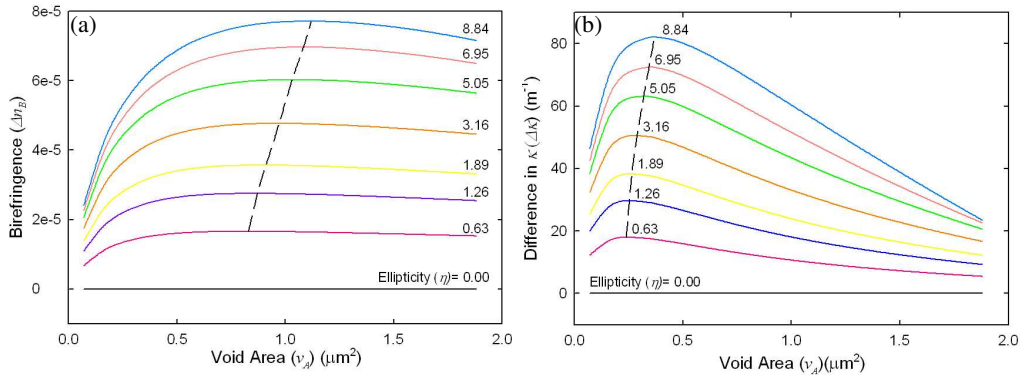


Fig. 3. (a) Birefringence and (b) difference in coupling coefficients as a function of void area for constant ellipticities. The dashed lines join the points of maximum birefringence and  $\Delta\kappa$ .

Figure 4 displays the absolute reflectivity for the two orthogonal states of linear polarisation as calculated from Eq. (3), as a function of the void area for grating lengths of 4, 6 and 8 mm. It can be seen that as  $A_v$  increases,  $R$  increases and saturates for all grating lengths. Because of the  $\tanh^2$  dependence of  $R$  on  $L$ , (shown in Eq. (3)) longer gratings saturate for smaller values of  $A_v$ , which can be visualized in Fig. 4(a). This leads to the difference in  $R$ , which can be seen in Fig. 4(b) reaching its maximum for smaller voids as the grating length is increased. It also leads to the magnitude of  $\Delta R$  decreasing as a function of grating length. Therefore, care must be taken when using Fig. 3(b) to design a grating for maximum difference in reflectivity (PDGS),  $\Delta R$ , as it only states the dimensions of the void required in order to maximize the difference, but the length must be adjusted carefully to minimize the effect of saturation of the absolute grating reflectivity. Carelessness will result in an optimum  $\Delta\kappa$ , but a near zero  $\Delta R$  as the gratings saturate in the linear regime.

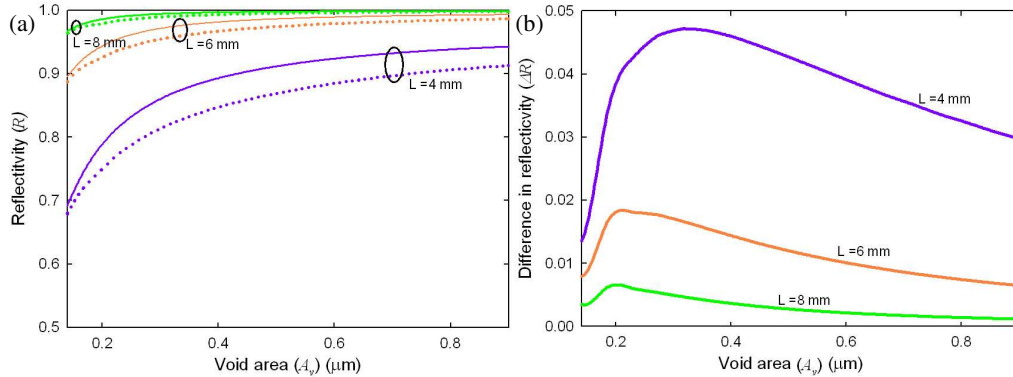


Fig. 4. (a). Absolute  $R$ , for two orthogonal states of linear polarization as a function of  $A_v$  for grating lengths of 4, 6, and 8 mm. Dotted lines represent the y-polarization and solid lines represent the x-polarization. (b) Displays the corresponding  $\Delta R$ .

### 2.3 Refining the model.

The effect of vertical offset of the PbP RIM was also explored, as this is the most difficult parameter to align during fabrication of the gratings and varies when writing gratings with different pulse energies due to self-focusing. Indeed all the gratings fabricated in this study had a measured vertical offset from the center of the core of order 0.3–1.4  $\mu\text{m}$ . It can be seen from Fig. 5(a), for a RIM with a vertical offset of 1.33  $\mu\text{m}$  from the center of the core that the energy distribution of the mode is localized to a much smaller degree in the vicinity of the void as compared to a non-offset RIM (Fig. 2(b)).

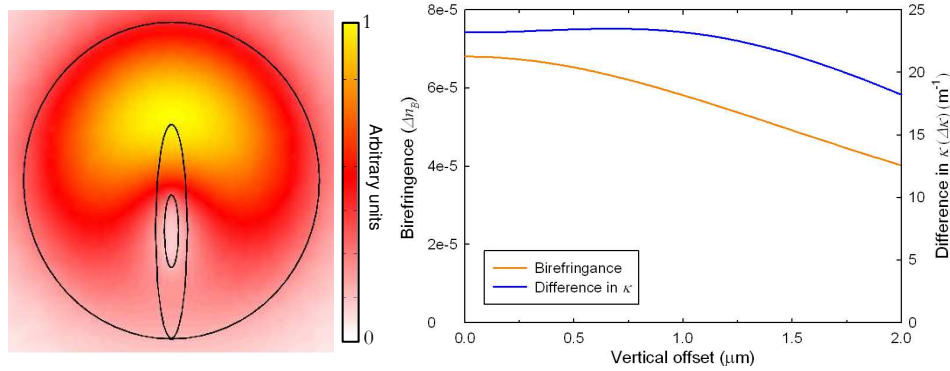


Fig. 5. (a) Energy flux profile when a PbP RIM is vertically offset in the core. (b)  $\Delta n_B$  and  $\Delta \kappa$  as a function of vertical offset of the PbP RIM.

It can be seen that as the offset increases,  $\Delta n_B$  decreases and  $\Delta \kappa$ , after initially being roughly constant, decreases as well. This is to be expected, as the RIM interacts with less of the energy in the mode and therefore has a weaker influence upon it. Therefore extra care must be taken to align the vertical axis of the grating with the center of the core in order to maximize the required parameters of the grating.

Now we turn to the effect of introducing an elliptically shaped densification around the void with dimensions  $h_d = 5.6 \mu\text{m} \times w_d = 0.9 \mu\text{m}$ , which are average values from the FBGs viewed. The values assumed for the difference in the refractive index of the densification,  $\Delta n_d$ , are an estimate and are slightly larger than values for waveguides written in bulk glasses because in our case there is much more substantial densification due to void formation. Values in the literature range from  $1 \times 10^{-3}$  up to  $5 \times 10^{-3}$  in one case [22], for waveguides, and therefore we assume that values of  $\Delta n_d$  could range from  $1 \times 10^{-3}$  for weak gratings to as much as  $5 \times 10^{-2}$  for strong gratings. The latter value is based on a calculation of the direct displacement of the material of the void into the densified region. The void was assumed to have an index of 1 which makes the index step  $\sim 0.45$  and therefore at least 1 order of magnitude greater than that of the densification. The densification was assumed to have a uniform refractive index profile which is not exact, but is a reasonable approximation. In addition,  $\Delta n_d$  was not rescaled to account for the duty cycle since this correction is negligible compared to the uncertainty in the actual value.

Figure 6 displays  $\Delta n_B$  and  $\Delta \kappa$  as a function of  $\Delta n_d$ . It can be seen from Fig. 6 that  $\Delta n_B$  and  $\Delta \kappa$  increase monotonically as a function of  $\Delta n_d$ , from values of  $6.4 \times 10^{-5}$  and  $52 \text{ m}^{-1}$  respectively when there is no densified shell, to  $8.9 \times 10^{-5}$  and  $98.7 \text{ m}^{-1}$  when a strong but realistic value of  $\Delta n_d = 1 \times 10^{-2}$  is implemented. This is an increase of 40 % and 90 % respectively. Also from Fig. 6, the power confined within the densified region increases as a function of the magnitude of the refractive index modulation. Therefore the increased birefringence and difference in  $\kappa$  are a result of the higher index densified region, drawing more of the energy in the mode in around the void, which makes the mode more sensitive to the impact on the birefringence and the difference in grating reflectivity of the void.

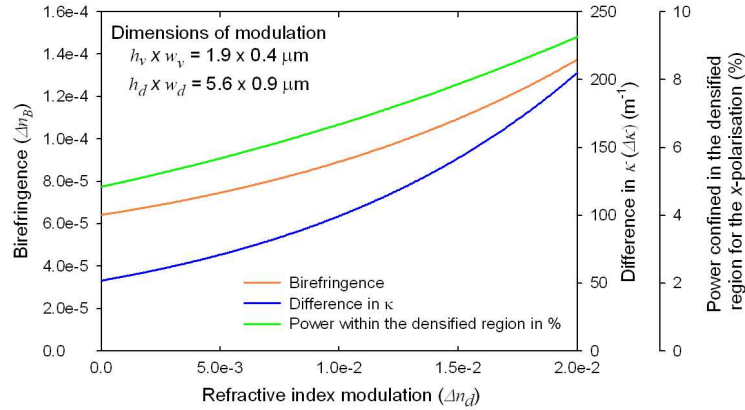


Fig. 6. Birefringence, difference in cross-coupling coefficient,  $\kappa$ , and power confined within the densified region as a function of  $\Delta n_d$ . The dimensions of the modulation used in the calculation are displayed in the figure.

From our calculations it can be seen that the birefringence and difference in grating strength between two orthogonally polarized modes are a direct result of the morphology of the refractive index modulations. The magnitude of the birefringence and the difference in grating strength are primarily influenced by the size and elliptical shape of the void as well as its position in the core and the refractive index contrast of the densified shell. We verified the assignment of the fast and slow axis and the deduction that the index modulation must be on average negative.

Previous work in femtosecond-laser-inscribed long period fiber gratings has demonstrated the presence of an asymmetrical increase in the radial core stress [23]. However that study was carried out in a pulse regime where melting and densification are the dominant effects and void formation was not present as in our case. From our experiments, it is difficult to separate the birefringence resulting from the stress from that of the morphology. A first principles model of the stress-induced birefringence is beyond the scope of this paper.

#### 2.4 Optimization of polarization dependent grating strength

In this section we optimize FBGs for maximum PDGS in order to use them as polarisation discriminators in fiber laser cavities. From Fig. 3(b) above, there is a maximum in the  $\Delta \kappa$  at different values of void area, for given void ellipticities. Therefore the ellipticity was first selected by choosing the appropriate focusing objective and then the pulse energy, which has been shown to be related to the void size and hence void area, in the 2D projection, was adjusted.

As outlined in the experimental section a 0.8 N.A., 20 $\times$  oil-immersion objective lens was used to write the FBGs. However the effective N.A. used was less than this as the 14.5 mm hard aperture of the lens was under filled with a  $\sim 5.3$  mm,  $1/e^2$  beam diameter. By using a low writing N.A., a high degree of ellipticity was ensured.

In order to vary the area of the void, we adjusted the writing pulse energy. It has been shown that the width of the micro-voids has a cube-root dependence on the writing pulse energy which can be approximated as linear for FBGs written with pulse energies far enough above threshold [21]. It follows that as the void width increases as a function of pulse energy, the void area will also increase.

A series of 5 mm long gratings were written with increasing pulse energies. The measured difference in linear reflectivity,  $\Delta R$ , between two orthogonal polarizations and the birefringence,  $\Delta n_B$ , for each grating is summarized in Fig. 7. It can be seen that  $\Delta R$  increases as a function of pulse energy before reaching a maximum of 14% for a writing pulse energy between 130 and 150 nJ.  $\Delta n_B$  can be seen to increase as a function of pulse energy as well

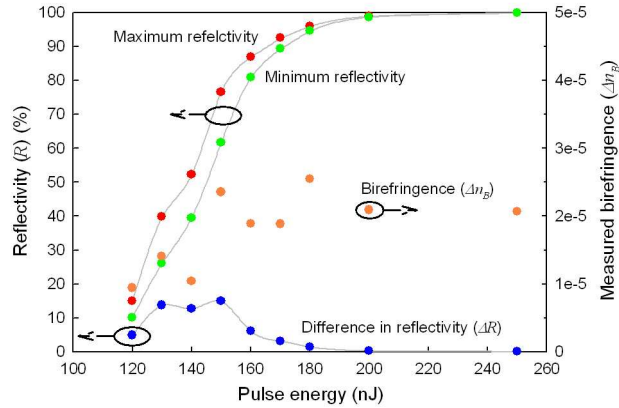


Fig. 7. Linear grating reflectivity for two orthogonal states of linear polarization, the difference between them and the birefringence as a function of pulse energy.

before reaching a maximum around 150-180 nJ. As the pulse energy is related to the void area as previously explained, the trends in  $\Delta n_B$  and  $\Delta R$ , at least qualitatively confirm the modeling in Figs. 3 (a) and 3(b) respectively. The maximum  $\Delta n_B$  and  $\Delta \kappa$ , corresponding to the maximum  $\Delta R$ , from the measurements, were  $2.5 \times 10^{-5}$  and  $59 \text{ m}^{-1}$  respectively. Since the average measured ellipticity of the voids for the FBGs displayed in Fig. 7 was 4.9 (measured from micrographs of FBGs similar to Fig. 1(b)), then from Figs. 3(a) and 3(b) the theoretical maximum values for  $\Delta n_B$  and  $\Delta \kappa$  for an ellipticity of 5.05, which is closest to our measurements, are  $6.0 \times 10^{-5}$  and  $63 \text{ m}^{-1}$  respectively. The theoretical and measured values are the same order of magnitude and in the case of  $\Delta \kappa$ , are consistent to within experimental uncertainty; however, the birefringence is still a factor of 2 greater in our simulations compared to the measurements. Approximately 20 % of this difference can be explained by the fact that the gratings displayed in Fig. 7 had an average vertical offset of the RIM from the center of the core of  $1.33 \mu\text{m}$  (taken from Fig. 5(b)). We attribute the rest of the discrepancy to the high uncertainty in the exact values of the simulation parameters and a possible contribution from stress. Finally, the magnitude of  $\Delta n_B$  observed in Fig. 7 is of the same order of magnitude as that observed in [1, 9].

### 2.5 Fiber lasers based on PDGS optimized PbP FBGs

In this section we investigate the effect of employing PbP FBGs optimized for maximum PDGS to fiber lasers, in order to create linearly polarized fiber lasers, without using extra components such as polarization maintaining fibers or polarization controllers. The fiber laser cavities used to test the effect of the FBGs on the lasers are depicted in Fig. 8. Cavity configuration (a) was used as a reference setup, while configurations (b)–(d) were used to investigate what effect each cavity component had on the polarization of the laser.

A 976 nm, single-mode fiber coupled laser diode with a maximum output power of 410 mW was used to pump each laser configuration through a wavelength division multiplexer (WDM). A 3 m long, low birefringence, erbium ( $\text{Er}^{3+}$ )-doped fiber was used in all cavity configurations. High reflector (HR) and output coupler (OC) gratings were written with a pulse energy of 140 nJ into SMF-28e in order to optimize the FBGs for maximum PDGS, as can be seen in Fig. 2, with lengths of 20 mm and 4 mm respectively for a 2<sup>nd</sup> order resonance at a Bragg wavelength of 1540 nm. As can be seen from Fig. 9(a), the optimized HR and OC are spectrally separated and in order to overlap them temperature tuning of the HR was used. For comparison, a non-optimized HR was written with pulse energies of 200 nJ, with a length of 5 mm, for a 2<sup>nd</sup> order resonance at a Bragg wavelength of 1525 nm. Transmission spectra of the FBGs used in the fiber lasers are presented in Fig. 9(a).

A polarization-independent bulk silvered mirror was used as a high reflector at normal incidence in several cavity arrangements to eliminate the effect of the HR on the laser's extinction ratio. Cavity configuration (a) was used as a control to observe the effect of the fiber on the laser's extinction ratio. Most cavity configurations were tested with both, a coiled and an uncoiled fiber. The three lasers with FBGs in the cavities, namely (b) (c) and (d), lased at a wavelength associated with the Bragg wavelength of the FBGs (see inset to Fig. 9(b)). No care was taken in aligning the fast or slow axes of the HR and OC for all lasers constructed with configuration (b).

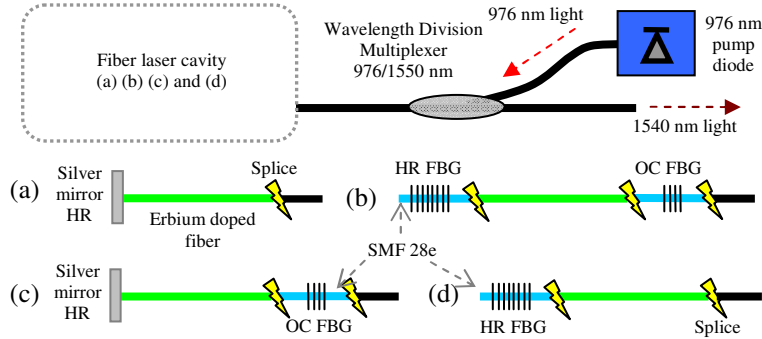


Fig. 8. Schematic of fiber laser architecture with various laser cavities. (a) HR silver mirror and a low reflecting splice as OC, (b) HR FBG and OC FBG, (c) HR Silver mirror and an OC FBG, (d) HR FBG and a low reflecting splice. Note: yellow lightning bolts represent splices.

The maximum output power of 62 mW with an optical to optical slope efficiency of  $(30 \pm 2) \%$  was observed with cavity configuration (d). This is to be expected as erbium is a high gain system that produces the greatest slope efficiencies with a low reflectivity value for the OC, which in this case was a few percent provided by the splice. The degree of polarization of each fiber laser was probed by collimating the output of the WDM, and then using a half-wave plate and a linear polarizer as an analyzer with the transmitted power measured on a photodetector. The extinction ratio (ER) used in this paper is defined as  $E.R. = -10 \log_{10}[P_{min}/(P_{max} + P_{min})]$ . Note: by this convention an unpolarized beam still has 50% of the power in one state of polarization which is an ER of 3 dB while a highly linearly polarized laser with 99.99 % of the light in a single state of linear polarization has an ER of 40 dB. The ERs of the four cavity configurations are summarized in Table 1 below.

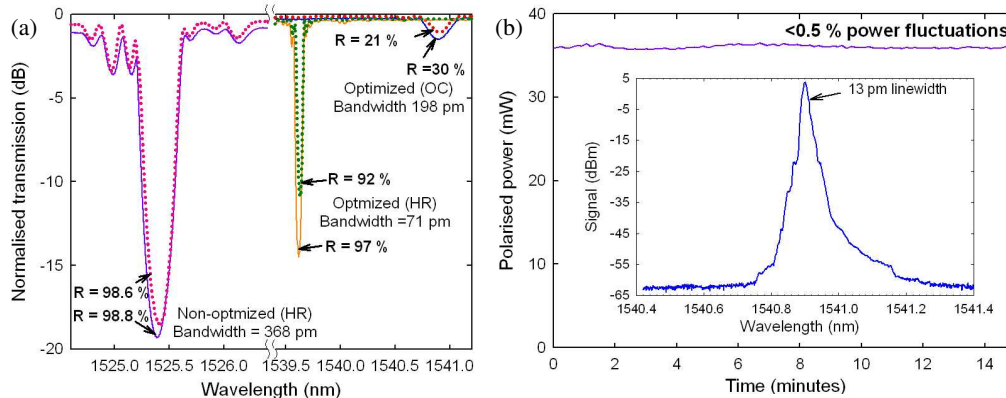


Fig. 9. (a). Transmission spectra for a PDGS optimized HR and OC and a non-optimized HR. The dotted curves correspond to light polarized parallel to the long axis of the RIMs while the solid curves correspond to light polarized perpendicular to the long axis of the RIMs. (b) Output power as a function of time for cavity configuration (b). Inset to (b) shows a typical laser spectrum from fiber lasers with cavity configurations (b), (c) and (d).

Table 1. Extinction ratio of 3 m long fiber lasers with the four cavity configurations shown in Fig. 8.

Cavity configuration	Extinction Ratio (ER) [dB (%)]			
	(a)	(b)	(c)	(d)
No coiling	3.2 ± 0.2 (52 ± 2)	30 (99.9)	32 (> 99.9)	5.3 (71)
100 mm diameter coil	4.0 ± 0.1 (60 ± 1)	34 (> 99.9)	-	29 (99.9)

It can be seen from Table 1, that when configuration (a) was used, i.e. no polarization discrimination implemented, the erbium doped fiber laser was unpolarized. This confirms that the erbium doped fiber and the bulk, silvered mirror as well as the WDM have no polarization dependence. In contrast, for the cases with PbP FBGs, which are polarization dependent, it can be seen that in all cases it is possible to achieve a highly linearly polarized fiber laser in a relatively long length of fiber. The ER increased for all cavity configurations when 100 mm diameter coiling of the fiber laser was implemented. We attribute this to induced polarization dependent losses in the coiled roll of fiber which aid in reducing the weaker lasing polarized mode, i.e. increasing the extinction ratio. The values for ER reported in the table above compare well to that published in [2] of 40 dB, however in that case the cavity was only 31 mm long (100 times shorter). A negligible reduction of the order of 0.2% in the maximum output power was observed when the coil was implemented. From the results in Table 1 for cavity configurations (c) and (d), it can be inferred that the OC has more impact on the final lasing state of polarization than does the HR, which can be explained by the two following arguments:

1. The output coupler is the last cavity element the laser light interacts with before it leaves the laser.
2. The difference in reflectivity, as a percentage, between the two Bragg wavelengths is greater for the OC than for the HR (see Fig. 9(a)).

All the cavity configurations outlined above were tested at elevated temperatures ranging from 40°C for stabilizing OCs, up to 150°C for tuning HRs, with no degradation of the performance of any laser after several on/off cycles of both pump power and temperature.

Figure 9(b) also shows the stability of cavity configuration (b) over a 15 minute period. It can be seen that there are negligible power fluctuations, mostly associated with instabilities in the pump laser diode. A similar level of stability was observed for all the lasers investigated.

In order to determine the effect of cavity length on the ER of the fiber laser, cavity configuration (b) was tested for a number of different lengths and the results are summarized in Fig. 10. Again no care was taken to align the axes of the HR and OC for any length of laser. It can be seen that for all lengths of the laser cavity tested the laser operated with an ER > 10 dB without coiling, which increased to a minimum ER of ~ 30 dB when coiling was implemented. The reduced ER for a cavity length of 5 and 10 m is attributed to a non-optimal

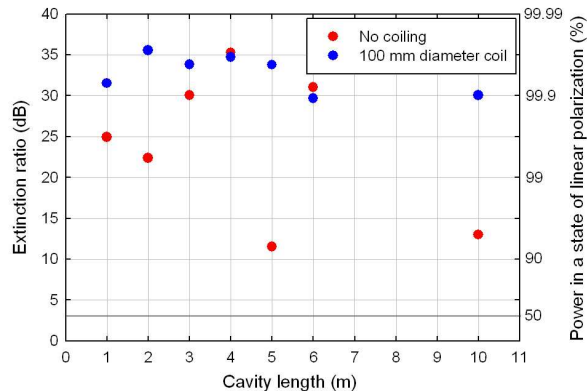


Fig. 10. ER for different cavity lengths for cavity configuration (b).

alignment of the axes of the two FBGs used for the cavity mirrors, allowing a greater degree of cross-talk between the two lasing states of polarization to occur. Although no care was taken in aligning the axes of the FBGs in any of the above outlined experiments, the ER of the laser depends on this alignment to some degree. These results clearly highlight that the cavity length does not significantly affect the ER of a fiber laser with FBGs that have been optimized for maximum PDGS.

The effect of aligning the grating axes of the HR and OC in configuration (b) was investigated by clamping the fiber on the cavity side of the OC and rotating the OC with respect to the cavity/HR. It was determined that the laser would lase with a constant maximum ER over a wide range of angles of rotation and only have a very low ER, i.e. be unpolarized, over a narrow range (20 degrees) of rotation corresponding to the axes being aligned at 45 degrees to one another. Therefore the ER of the laser can not be improved by aligning the grating axes more carefully unless the constructor was unfortunate enough to splice the gratings to the laser initially, such that the axes were aligned in the narrow range of angles around 45 degrees with respect to each other and hence the laser operates unpolarised.

When coiling diameters smaller than 100 mm were implemented, the extinction ratio of the lasers was observed to decrease in almost all cases. We attribute this to the added affect of twist induced birefringence which we predominantly managed to avoid when coiling to 100 mm diameters. Furthermore the exact extinction ratio fluctuated wildly upon recoiling as the precise amount of twist varied from one coiling to another.

Cavity configuration (d) was also implemented with the non-optimized HR shown in Fig. 9(a) and the resulting ER was 3.16 dB without coiling and 4.43 dB with coiling. Therefore it is clear that an optimization of the PDGS is of utmost importance in order to realize a linearly polarized fiber laser in low birefringence, non-polarization maintaining fiber.

### 3. Conclusion

We have shown that the PDGS and birefringence associated with PbP FBGs inscribed using femtosecond lasers are strongly dependent on the ellipticity, size and vertical positioning of the micro-voids in the core of the optical fiber. The average refractive index after inscription of a PbP FBG with a femtosecond laser is lower than that of pristine SMF 28e which is consistent with the formation of micro-voids. For the first time, we have associated a grating axis with a polarization-dependent transmission spectrum. In particular, the slow axis corresponds to light polarized parallel to the long axis of the elliptical RIM while the fast axis is orthogonal to it.

Fiber lasers were constructed with PbP FBGs optimized for maximum PDGS and were observed to lase fully linearly polarized, even while employing a low birefringence cavity. It was observed that, by coiling each of the cavities the extinction ratio could be increased above 30 dB. The lasers extinction ratio was determined to be nearly independent of cavity length and therefore laser cavities as long as 10 m can still provide a linearly polarized output if the

gratings are optimized. This is ideal in the case of most high power fiber lasers which are typically several meters in length. Grating optimization is a prerequisite to realizing linearly polarized fiber lasers in this case.

The presented types of fiber lasers are greatly simplified as they remove unnecessary components from the polarized fiber laser setup, such as external polarization controllers, bulk optics and polarization maintaining fibers. This increases the robustness of the systems which makes them applicable to medical and airborne environments and greatly reduces the costs.

### **Acknowledgments**

The authors would like to acknowledge the help of Dr Eric Mägi and Dr Jeremy Bolger in obtaining accurate polarization dependent measurements of fiber Bragg gratings. This work was produced with funding from the Australian Research Council under the ARC Centres of Excellence and LIEF programs and the German Federal Ministry of Education and Research (BMBF). Jens Thomas acknowledges funding by the DAAD, grant D/0846673.